An Improved Method for Characterizing Plasma Density Profiles Using Angular Filter Refractometry

Introduction

The measurement of plasma density profiles is important to many areas of high-energy-density (HED) laser–plasma interactions.[1] Quantitative analysis of large HED plasmas has historically been challenging in the range of electron densities near 10^{20} to 10^{21} cm^{-3}. This density range is too low for x-ray probing techniques[2] and too high for most optical techniques. The large integrated phase obtained with optical probes makes it difficult to quantitatively measure the density profile when using typical interferometric techniques.[3,4] A variety of techniques do exist by which one can attempt to measure this region, but each technique has limiting drawbacks.[5]

A novel diagnostic called angular filter refractometry[6] (AFR) can enable one to characterize plasma density profiles up to densities of 10^{21} cm^{-3} by measuring the refraction angle of a probe beam passing through the plasma. The refractive information can be analyzed to characterize the density profile of the plasma. Previously used methods of reducing this experimental data to produce a plasma density profile were cumbersome and at times oversimplified the density profile,[6,7] both resulting in higher uncertainties.

A new method of analysis has been developed that involves simulating the AFR diagnostic response. A density profile described by seven parameters is used to generate synthetic AFR data, and a quantitative method for defining the degree of similarity between synthetic and observed AFR data provides feedback for subsequent iterations. The synthetic density profile is altered using an intelligent annealing algorithm to iteratively converge upon a solution whose resulting synthetic AFR data closely matches observed AFR data.

This approach has multiple advantages over other methods of analysis: It requires minimal user interface, which eliminates human error that exists from direct manipulation of the observed data. It lends itself to a statistical uncertainty calculation based on χ^2 statistics, allowing one to assess quantitative uncertainties. The resultant density profile, by nature of it being analytic, provides smooth gradients free of noise for scale-length calculations.

In this article, the process by which the synthetic density can be matched to observed AFR data is explained in detail. The different causes of uncertainty specific to this approach and to the diagnostic in general will be described.

Angular Filter Refractometry

The AFR diagnostic is part of the fourth-harmonic (4ω) probe system[8] on LLE's OMEGA EP laser.[9] The 4ω probe is created from the conversion of a Nd:glass laser pulse to its fourth harmonic ($\lambda_p = 263$ nm) and has a pulse width of 10 ps with 20 mJ of energy. Figure 149.44 shows a conceptual schematic for the AFR diagnostic. The red lines represent the path of the undisturbed probe beam. The beam has a diameter of 3.5 mm and passes through the target chamber center (TCC), where the plasma will be created. The probe is collected at $f/4$ and transported more than 4 m to the diagnostic table.
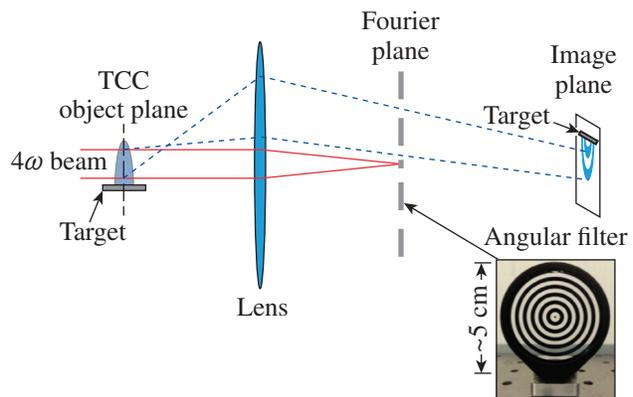
E22129JR

Figure 149.44
A simplified schematic of the angular filter refractometry (AFR) diagnostic. Unrefracted probe rays (red lines) are blocked by the opaque center of the angular filter. Refracted probe rays (dashed blue lines) hit or miss the filter based on their refraction angles through the plasma. The filter casts shadows corresponding to specific refraction angles that are observed on the image plane. TCC: target chamber center

The TCC plane is image relayed to a charge-coupled–device camera with a resolution of 5 μm over a 5-mm field of view in the object plane.[8]

An angular filter is placed at the focus of the unrefracted probe beam, or the Fourier plane.[10] The filter consists of a central opaque dot and oscillating transmissive and opaque rings (Fig. 149.44). The unrefracted probe is stopped by the central dot. In the presence of a plasma, refracted rays (dashed blue lines) will fill a larger area of the angular filter. The opaque regions of the filter block bands of refraction angles, thereby casting shadows in the image plane. Because the angle of refraction of a probe ray is directly proportional to its radial location in the Fourier plane, the shadows on the image plane have contours of constant refraction. To calibrate the specific angular cutoffs, a plano-concave lens was placed at TCC, allowing one to deduce the refraction angle (θ) as a function of displacement (r) from the optical axis in the Fourier plane. For a more-detailed description of the diagnostic, see Ref. 6.

Figure 149.45 shows an example of an AFR image measured from a 250-μm-thick CH target that was ablated by four UV (λ = 351 nm) laser beams with a total of 9 kJ of energy in a
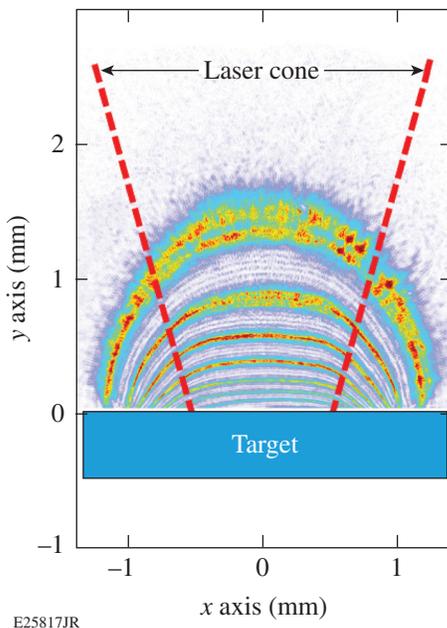

Figure 149.45
A laser irradiates a CH target and creates an axisymmetric plasma plume. The angular filter blocks certain refractive angles, resulting in the banded image.

2.5-ns square pulse focused to an 800-μm-diam spot that contained 95% of the energy. The target surface was set to $y = 0$, and the plasma expanded in the positive y direction away from the target. The refraction bands produced by the AFR diagnostic show the shape of the expanding plasma plume.

Analysis

1. Creating a Synthetic AFR Image

The AFR images are analyzed by comparing them to a synthetic image generated with a model 3-D plasma density n_e (x,y,z). (Note: All following references to n_e assume a dependence on x,y,z.) A typical HED laser-plasma plume from a planar target can be modeled by a super-Gaussian parallel to the target and exponential normal to the target.[11] The 3-D density profile was assumed to be axisymmetric along the target normal. The behavior along the target normal at the plasma's center is modeled as

$$n_e(0,y,0) = n_0 \cdot \left[A \cdot \exp\left(\frac{-y}{L_{y1}}\right) + (1-A) \cdot \exp\left(\frac{-y}{L_{y2}}\right) \right], \quad (1)$$

where n_0 is the peak density and A assigns relative strength to two exponential profiles with scale lengths L_{y1} and L_{y2}. This allows the profile to adapt to a decreasing scale length as typically occurs close to the target surface. The full density profile, including the transverse dimension, is

$$n_e(x,y,z) = n_e(0,y,0)$$
$$\times \exp\left\{ -\left(\frac{x^2+z^2}{L_{xz}^2}\right)^{\frac{1}{2}\left[c_1 - c_2 \cdot \ln(c_3 \cdot y)\right]} \right\}, \quad (2)$$

where L_{xz} is the scale length in both x and z and the parameters c_1, c_2, and c_3 (representing two independent parameters) are used to define the order term for the super-Gaussian profile. The order term was empirically found so one could accurately match experimentally observed AFR contours. Equations (1) and (2) together form the seven-parameter function that constitutes the synthetic 3-D density. Figure 149.46(a) shows the density solution to the experimental AFR map shown in Fig. 149.45, where the deduced density spans two orders of magnitude (10^{19} to 10^{21} cm^{-3}).

With the probe propagating in the z direction, the accumulated phase of the probe ray passing through the plasma is related to the 3-D plasma density according to
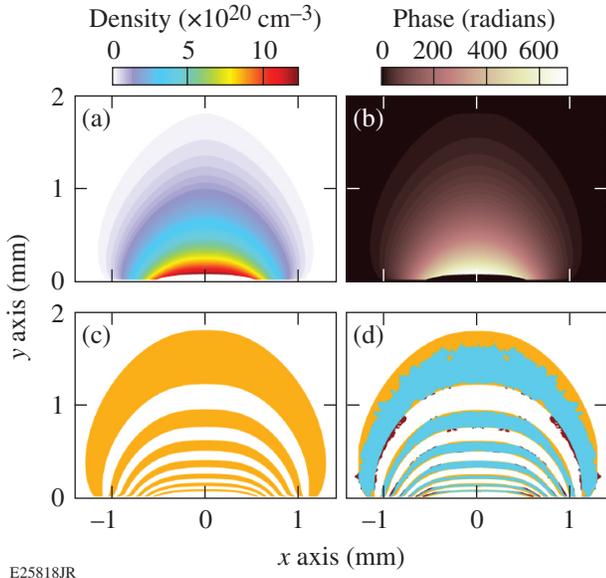
E25818JR

Figure 149.46
(a) A 2-D slice of a 3-D axisymmetric synthetic density profile generated from the density function described by Eq. (2). (b) The integrated phase accrued by the probe passing through the synthetic plasma. (c) The synthetic AFR image made by extracting refraction information from the phase map following Eq. (4) and eliminating angles blocked by the filter. (d) A visual overlay of the synthetic (orange) image and experimental (red) image. Blue indicates where the profiles overlap.

$$\phi(x,y) \approx \frac{\pi}{\lambda_p n_c} \int_{-\infty}^{+\infty} n_e(x,y,z)\, dz\,[\text{rad}], \qquad (3)$$

where λ_p is the probe-laser wavelength (263 nm) and $n_e \ll n_c$, where $n_c = 1.1 \times 10^{21} / \lambda_{p,\mu m}^2 = 1.6 \times 10^{22}$ cm^{-3} is the critical plasma density for the probe laser. Figure 149.46(b) shows the integrated phase of the density profile in Fig. 149.46(a), where changes in x and y along the ray path are ignored. The angle of refraction of a probe ray exiting the plasma is calculated from the transverse gradient of the accrued phase:

$$\theta(x,y) = \frac{\lambda_p}{2\pi} \sqrt{\left(\frac{\partial\phi}{\partial x}\right)^2 + \left(\frac{\partial\phi}{\partial y}\right)^2}\,[\text{rad}]. \qquad (4)$$

From the calculated 2-D refraction map, a filter function based on the calibration is applied that creates a synthetic AFR image comparable to that measured in the experiment [Fig. 149.46(c)].

2. Simulated Annealing

An iterative solver alters the parameters of the synthetic density function to optimize the match between the synthetic and experimental AFR images. The quality of the match is based on the location of the edges of the bands. This was accomplished by taking many radial lineouts of the synthetic and experimental AFR images and finding the position of the edges of the bands at each angle [Fig. 149.47(a)]. The edge locations in the experimental images were found by applying a 20% intensity threshold to the normalized data, which eliminated most noise without notable alterations to the bands' behavior and size. Figure 149.47(b) compares the thresholded experimental edges to the synthetic AFR edges. The squared differences of the locations between the synthetic and experimental AFR band edges were averaged over the entire image:

$$m = \sum_{n=1}^{14} \sum_{r=1}^{100} (E_{n,r} - S_{n,r})^2, \qquad (5)$$
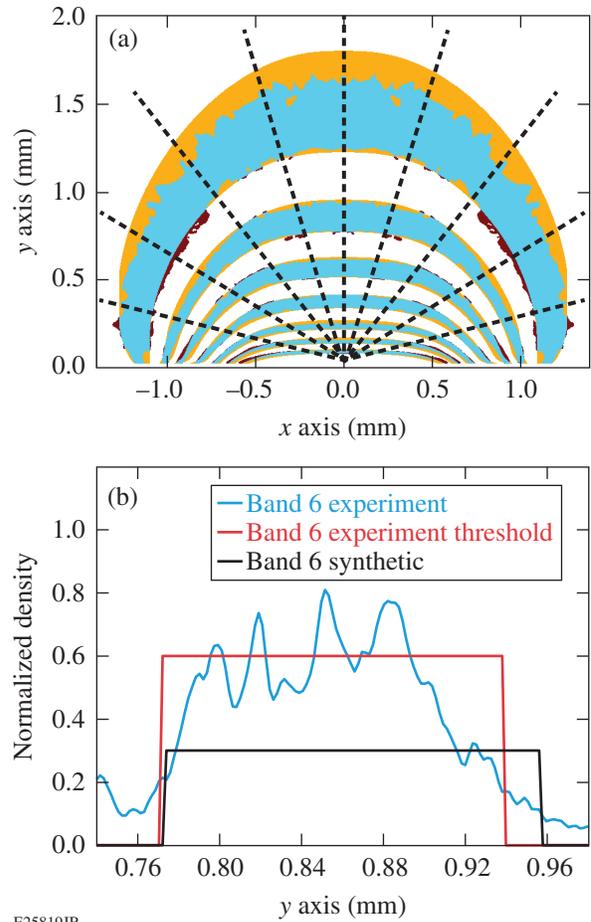

E25819JR

Figure 149.47
(a) The algorithm draws lineouts from the center of the target surface and finds the edges of the experimental and synthetic bands on those lines. (b) A lineout of the sixth band (counting from the bottom) taken along $x = 0$. A threshold was applied to the experimental data to eliminate noise.

where $E_{n,r}$ and $S_{n,r}$ are the edge locations of the experimental and synthetic bands, respectively, at an edge n and an angle r. All 14 edges were examined at a large number of angles so that slight fluctuations at some points in the experimental AFR image do not dominate the match (Fig. 149.47).

The solver incorporates the simulated annealing[12] (SA) algorithm to systematically alter the variables of the density function until a global minimum for m in the parameter space is found. An SA algorithm was chosen because of its ability to find a global minimum in a large parameter space [seven parameters; see Eq. (1)], where many local minima exist. Figure 149.48 displays the logical flowchart that the SA algorithm follows. The SA algorithm takes an initial user-defined density guess n_i, generates the synthetic AFR image, and calculates m_i. The density is then perturbed by Δn and a new match parameter $m_{i+\Delta n}$ is calculated. If $m_{i+\Delta n}-m_i < 0$, the new profile is accepted and $n_i + \Delta n$ becomes the new n_i. If $m_{i+\Delta n}-m_i > 0$, the new profile is considered for rejection, although there is a chance that it may be accepted.

Accepting a poorer match over a superior one allows the profile to escape from local minima enroute to the final solution. The range over which parameters' values are generated and the likelihood of accepting a poorer match decrease at later iterations[13] so that the algorithm focuses around a nearby solution. After a set number of runs, the SA algorithm resets the range of parameters in the search and the likelihood of accepting a
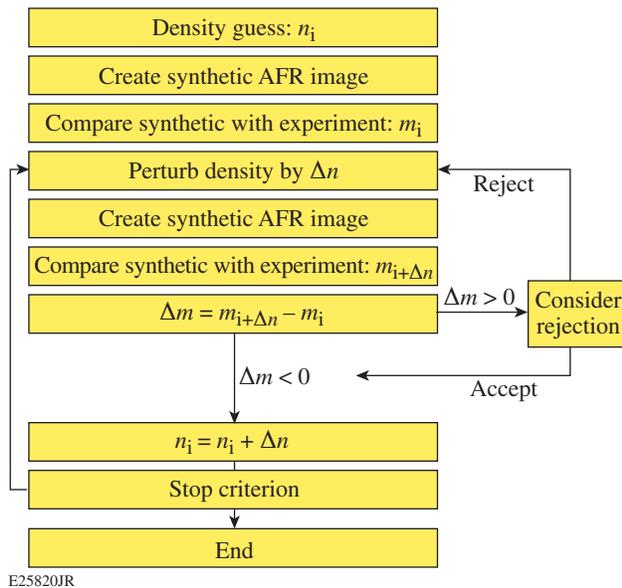
poor match. Repeating this process numerous times makes it unlikely for the algorithm to get stuck in a local minimum. The simulated annealing algorithm terminates when a chosen number of iterations pass without a new best match being discovered (stop criterion). At this point the profile corresponding to the lowest calculated match is returned by the algorithm. Figure 149.49(a) shows how a single simulating annealing algorithm closes in on its results. Occasionally it escapes its local minimum and finds a new one, trending toward the optimal value. The process of escaping a local minimum can be seen more clearly in Fig. 149.49(b).
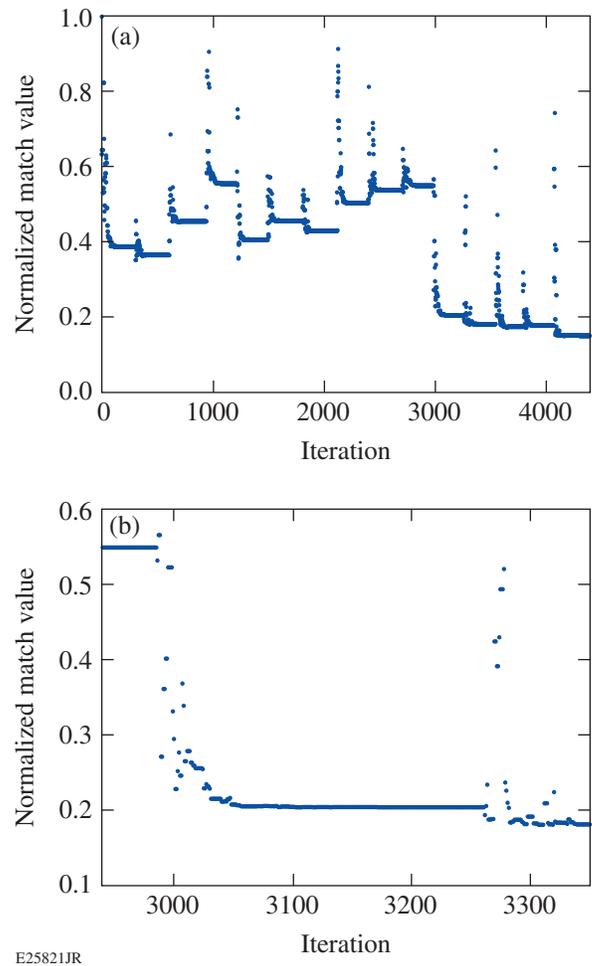

E25821JR

Figure 149.49
(a) The normalized match value m is plotted over a single simulating annealing run while modifying the parameters simultaneously. The long stretches of constant value represent local minima, which are typically escaped after first passing through inferior values. (b) A closer look at a certain portion of the run shows that the normalized value decreases sharply over 50 iterations that accept multiple poorer matches. After a long stretch in a local minimum, the algorithm begins accepting poorer matches again and then quickly finds a new lowest match value.

E25820JR

Figure 149.48
A flowchart describing simulated annealing.

This solver utilizes a series of SA algorithms that focus on particular groupings of parameters rather than one SA algorithm that modifies all parameters simultaneously. One group contains parameters that primarily affect the heights of the bands (n_0, A, L_{y1}, and L_{y2}); the other group contains parameters that primarily affect the behavior of the bands near the target surface (L_{xz}, c_1, c_2, and c_3). The SA algorithms are run in an alternating cycle on each parameter group, increasing the demand for accuracy the longer each group goes unaltered. The solver reaches the stop criterion when a certain number of iterations on both parameter groups pass without improving the match. This approach converges on a good match nearly twice as quickly as using one SA algorithm on all parameters. After the run is complete, a simple local neighborhood search is executed to fine-tune the answer.

Uncertainty Analysis

Three primary sources of uncertainty exist in the analysis. The first source is the statistical uncertainty in the match, which was accounted for by testing the χ^2 statistic.[14] A second source resides in the unknown integration constant in calculating phase from the angle of refraction [Eq. (4)]. The final source of uncertainty comes from a systemic left–right asymmetry in the AFR diagnostic presumed to be related to an optical aberration in the system. All three uncertainties are quantitatively accounted for and added in quadrature.

1. Statistical Uncertainty

The uncertainty related to the sensitivity to fit is calculated as

$$\Delta n_{\text{stat}} = \pm \sqrt{\left(\frac{dn_e}{dp_1}\right)^2 \sigma_{p1}^2 + \left(\frac{dn_e}{dp_2}\right)^2 \sigma_{p2}^2 + \dots}\ [\%], \quad (6)$$

where dn_e/dp is the derivative of the density function with respect to parameter p and σ_p is the uncertainty in p. The uncertainty in each parameter is determined using χ^2 statistical testing, which describes the similarity between theoretical and observed data. For this data, the χ^2 value is

$$\chi^2 = \sum_{n=1}^{14} \sum_{r=1}^{100} \frac{(E_{n,r} - S_{n,r})}{\alpha^2}. \quad (7)$$

This equation is the match value m divided by α^2, which represents the experimental noise, or the observed data that *cannot* be fit by the theoretical model. This means that m_{min}

represents the degree of noise for a given experimental AFR image, so $\alpha^2 = m_{\text{min}}$.

The uncertainty in each parameter is related to the way it alters the behavior of χ^2 around χ^2_{min}. Altering the parameters around their best-fit values increases χ^2, indicating a lower probability that these parameter values are correct.[14] A confidence interval[15] ΔS is defined to describe the increase to χ^2_{min} that would result in an N-percent certainty that the solution lies within ΔS (Ref. 5). Each parameter is individually altered until $\chi^2 = \chi^2_{\text{min}} + \Delta S$; the boundaries of this window represent the uncertainty in the parameter, σ. This was factored back into Eq. (6) to find the uncertainty in density. Because χ^2 is inversely proportional to m_{min}, Δn_{stat} will be larger for profiles whose best matches are not as strong. The calculated uncertainty map from χ^2 statistics for the case in Fig. 149.46 is shown in Fig. 149.50(a).
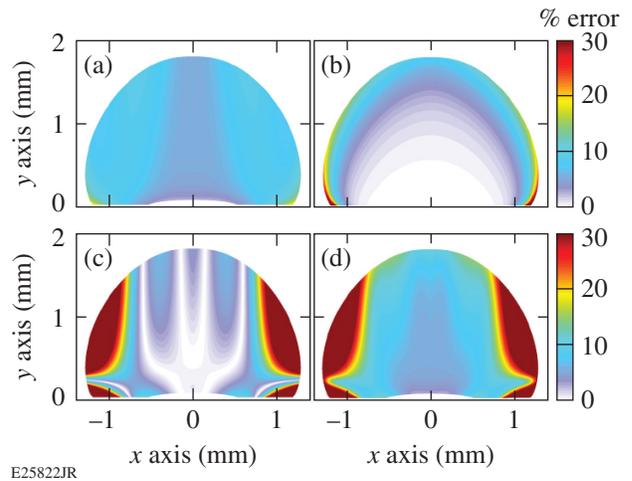
Figure 149.50
(a) The statistical uncertainty map corresponding to the density function. (b) The degenerative uncertainty. Note that the color bars cut off at 30% but at one point are as high as 100%. (c) The left–right uncertainty. Note that the color bars cut off at 30%, but uncertainties at the outer regions get higher. (d) The combined uncertainty.

2. Degenerative Uncertainty

The next source of uncertainty is related to the fact that the AFR diagnostic measures refraction, which is proportional to the gradient of the plasma density, or phase. The phase is proportional to the integration of refraction plus an integration constant (c) allowing for degenerate solutions. The value of c is a source of uncertainty in the density since changing c does not change the AFR image; therefore, boundary conditions must be established.

The main physical boundary condition on the density function is that density must fall to zero away from the target surface. The lowest density that contributes to the AFR image lies somewhere along the outer band's edge. This value must be non-negative, which gives a lower bound for c (negative value). Positive values for c violate the boundary condition of density going to zero without the introduction of additional gradients that exist outside the outermost band that are smaller than measurable by the AFR diagnostic.

There is no way to define the upper bound for c, so for testing purposes, the maximum shift to the density in either direction was taken to be the largest downward shift possible. A density function with over 20 parameters was used to create test AFR images. Those AFR images were treated as experimental ones and run through the iterative solver. The statistical uncertainty and degenerative uncertainty combined were always able to encompass the percent difference between the test cases and the corresponding optimized synthetic densities, proving the validity of these uncertainty calculations.

The corresponding uncertainty can be described by [Fig. 149.50(b)]

$$\Delta n_{\mathrm{deg}} = \pm \frac{c}{n_{\mathrm{e}}} [\%].\tag{8}$$

3. Asymmetry Uncertainty

There is a consistent left–right asymmetry in all AFR images. In theory the plasmas should be approximately axisymmetric due to nearly axisymmetric illumination, so it is believed that this asymmetry is symptomatic of an aberration in the probe beam. Efforts to model the presumed aberration were unsuccessful; therefore, it is accounted for as a source of uncertainty. Optimizations are run separately on the left and right sides of each shot and the solution is taken to exist somewhere within the percent difference between the resulting densities. This percent difference contributes to the uncertainty [Fig. 149.50(c)]:

$$\Delta n_{\mathrm{lr}} = \frac{\left| n_{\mathrm{left}} - n_{\mathrm{right}} \right|}{1/2 \times \left(n_{\mathrm{left}} + n_{\mathrm{right}} \right)} [\%].\tag{9}$$

Discussion

The total uncertainty is generated by adding the three separate uncertainty sources in quadrature.[16] The uncertainty calculations for the far left and right edges exceed 100% because

of the asymmetry. Over a large region of interest, the central two-thirds of the profile has an uncertainty of under 20%. The uncertainty along the target normal is under 10%.

The use of an analytic density function is an additional benefit to this analysis method. It facilitates an accurate calculation of the density scale lengths caused by the smoothness of the density derivative. This results in a low uncertainty for scale length. The scale length can be calculated as

$$L_y = \mp n_{\mathrm{e}} \left[\frac{\mathrm{d} n_{\mathrm{e}}}{\mathrm{d} y} \right]^{-1}.\tag{10}$$

Figure 149.51 shows the density and scale length of the plasma analyzed throughout this article along the target normal. Note that the uncertainty increases as the plasma is farther from the target surface but does not exceed 10%.
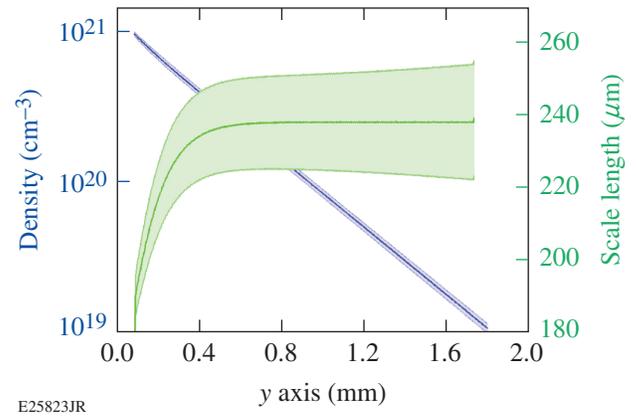

E25823JR

Figure 149.51
The blue line is the plasma density profile along the target normal at the center of the plasma profile ($x = 0$) measured from the AFR data shown in Fig. 149.45. The original target surface is located at $y = 0$. The green curve is the corresponding scale length. The uncertainty in scale length increases with y but is under 10% at all points.

Conclusion

A new method of analyzing data from the AFR diagnostic has been developed. A seven-parameter density profile was used to produce synthetic AFR images, and an iterative solver was developed that could successfully match synthetic data to experimental AFR images. A 2-D uncertainty map for the 3-D density was presented that has an uncertainty of less than 10% in the region of interest.

Several future improvements could increase the accuracy of this analysis. By adding more variables to the density function, it will have more flexibility to match the experimental AFR images, therefore improving the model fit. This would, however, be gained at the cost of computer run time. The degeneracy uncertainty could be erased completely if a boundary condition was known. This could be accomplished, for example, by measuring phase in the low-density regions using simultaneous interferometry. If the asymmetry was caused by an aberration, it could be largely reduced or eliminated by successful modeling the aberration on the probe beam, or experimentally fixing the aberration.

ACKNOWLEDGMENT

REFERENCES

1. National Research Council (U.S.) Committee on High Energy Density Plasma Physics, *Frontiers in High Energy Density Physics: The X-Games of Contemporary Science* (The National Academies Press, Washington, DC, 2003).

2. S. H. Glenzer, G. Gregori, F. J. Rogers, D. H. Froula, S. W. Pollaine, R. S. Wallace, and O. L. Landen, Phys. Plasmas **10**, 2433 (2003).

3. R. Benattar and C. Popovics, J. Appl. Phys. **54**, 603 (1983).

4. R. J. Noll *et al.*, Appl. Opt. **25**, 769 (1986).

5. R. S. Craxton, F. S. Turner, R. Hoefen, C. Darrow, E. F. Gabl, and Gar. E. Busch, Phys. Fluids B **5**, 4419 (1993).

6. D. Haberberger, S. Ivancic, S. X. Hu, R. Boni, M. Barczys, R. S. Craxton, and D. H. Froula, Phys. Plasmas **21**, 056304 (2014).

7. S. Ivancic, D. Haberberger, H. Habara, T. Iwawaki, K. S. Anderson, R. S. Craxton, D. H. Froula, D. D. Meyerhofer, C. Stoeckl, K. A. Tanaka, and W. Theobald, Phys. Rev. E **91**, 051101(R) (2015).

8. D. H. Froula, R. Boni, M. Bedzyk, R. S. Craxton, F. Ehrne, S. Ivancic, R. Jungquist, M. J. Shoup, W. Theobald, D. Weiner, N. L. Kugland, and M. C. Rushford, Rev. Sci. Instrum. **83**, 10E523 (2012).

9. J. H. Kelly, L. J. Waxer, V. Bagnoud, I. A. Begishev, J. Bromage, B. E. Kruschwitz, T. J. Kessler, S. J. Loucks, D. N. Maywar, R. L. McCrory, D. D. Meyerhofer, S. F. B. Morse, J. B. Oliver, A. L. Rigatti, A. W. Schmid, C. Stoeckl, S. Dalton, L. Folnsbee, M. J. Guardalben, R. Jungquist, J. Puth, M. J. Shoup III, D. Weiner, and J. D. Zuegel, J. Phys. IV France **133**, 75 (2006).

10. J. W. Goodman, *Introduction to Fourier Optics* (McGraw-Hill, New York, 1968).

11. M. Murakami *et al.*, Phys. Plasmas **12**, 062706 (2005).

12. S. Kirkpatrick, C. D. Gelatt, Jr., and M. P. Vecchi, Science **220**, 671 (1983).

13. S. Nozaki *et al.*, Rev. Sci. Instrum. **73**, 3198 (2002).

14. N. Bobroff, Rev. Sci. Instrum. **57**, 1152 (1986).

15. M. Lampton, B. Margon, and S. Bowyer, Astrophys. J. **208**, 177 (1976).

16. J. R. Taylor, *An Introduction to Error Analysis*, 2nd ed. (University Science Books, Sausalito, CA, 1982).